What is the Altitude of Thermal Equilibrium?

W.K. Peterson [1†], Naomi Maruyama[1], Phil Richards[2†], Philip J. Erickson[3], Andrew B. Christensen[4†], and Andrew W. Yau[5]

1: LASP, University of Colorado, Boulder
2: George Mason University, Fairfax Virgina
3: Haystack Observatory, Massachusetts Institute of Technology, 99 Millstone Road, Westford MA
4: Aerospace Corporation Retired, 2350 East El Segundo Blvd, El Segnundo CA
5: University of Calgary, Calgary, Alberta Canada
†: Retired

Key Points:

1. Thermal equilibrium is postulated to be attained at the lowest altitude heated by photoelectrons.
2. Quantitative understanding of thermal equilibrium requires observations that validate models.
3. There is an ongoing community need for simultaneous neutral, ion, and electron temperature profiles below 140 km altitude.

Abstract

Thermal equilibrium in planetary atmospheres occurs at altitudes where the ion, electron, and neutral temperatures are equal. Thermal equilibrium is postulated to occur in the collision-dominated lower ionosphere. This postulated altitude is above the lower boundary of all empirical models of planetary ionospheres. Physics-based model predictions of the altitude can not be validated due to a lack of adequate simultaneous observations of temperature profiles. This study presents temperature profiles from simultaneous observations on Atmosphere Explorer–C below 140 km and quiet-time neutral observations from TIMED/GUVI over Millstone Hill. These are compared with profiles from physics-based models with a discussion of their respective limitations. We conclude that there does not yet exist a quantitative understanding of the ion, electron, and neutral thermalization processes in low-altitude planetary ionospheres. Progress on this topic requires an adequate database of simultaneous ion, electron, and temperature profiles in the 110 to 140 km altitude range.

Introduction

The sub-auroral / mid- and low- latitude ionosphere is primarily created by the photoionization of neutral atmospheric gases by solar EUV and soft X-ray radiation below 120 nm. Approximately half the solar EUV energy is deposited in the ion states, and the remainder is carried by energetic photoelectrons. Much of the chemical energy deposited in the ions by photoionization leads to the heating of neutral particles through chemical reactions (Richards, 2012). Since the amount of heating per neutral gas particle increases with altitude, the neutral gas

temperature also increases with altitude until it is ultimately limited by downward heat conduction.

Quantitatively understanding the production and thermalization of photoelectrons has been a goal of space physicists since the dawn of the space age (for recent perspectives, see Peterson 2021 and Richards 2022). Photoelectrons are a significant source of ionization throughout the ionosphere, and they become the dominant ionization source below about 180 km altitude, as the softer EUV component is increasingly attenuated by absorption. The photoelectrons lose their energy in a cascade process involving the excitation and ionization of neutral species, and they eventually join the thermal electron population. At low energies, the photoelectrons heat the existing thermal electron population. Then, the thermal electrons lose their energy to the ions and neutrals. As a result, thermal electrons are usually hotter than ions, which are hotter than the neutrals. However, at low enough altitudes, where the neutral density is so much greater than that of the ions and electrons, cooling rates are so high that the ion, electron, and neutral temperatures are expected to be practically equal; i.e., in thermal equilibrium.

Below the altitude of thermal equilibrium, photoelectrons continue to be produced and thermalized. The resulting electron temperature in this collision-dominated environment will be slightly higher than the ion and neutral temperatures, but these temperature differences are beyond any realistic measurement capability. Indeed, even at night, EUV emissions from stars, galaxies, and sunlight resonantly scattered from the upper atmosphere generate small numbers of photoelectrons.

Photochemical equilibrium, where ions and electrons recombine locally and the different ion and neutral species undergo charge exchange reactions to attain chemical equilibrium, is well-known to occur below about 200 km altitude on Earth at solar minimum. This has been confirmed by numerous satellite measurements. On the other hand, thermal equilibrium, where the neutral, ion, and electron temperatures are approximately equal, is postulated to occur at some altitude below ~140 km on Earth and Mars. As discussed below, both planets have a relative lack of in-situ observations in this critical region. The altitude of thermal equilibrium delineates where energy input to the neutral atmosphere from solar EUV irradiance is small relative to the heat capacity of the thermospheric neutral gas. Below this altitude, neutrals can be heated by other processes, including gravity waves and solar UV absorption. Another low-altitude heat source is atomic oxygen produced in the thermosphere by photodissociation of O_2. The atomic oxygen so produced cannot recombine in the thermosphere, and it diffuses down to the mesosphere, where it recombines into O_2 via 3-body reactions that release energy. The energy exchange processes determining the neutral temperature at the mesopause (~80 km on Earth) and above is a topic of current community interest (e.g., Sarris et al. 2020, Heelis and Maute 2020, Palmroth et al. 2021, and Jones et al. 2022).

Systematically investigating and modeling the processes that heat neutrals above the mesopause and below the altitude of thermal equilibrium requires a robust understanding of the upper boundary conditions, such as ion, electron, and neutral temperature profiles in the 110-130 km range. Thus, to understand neutral heating at these altitudes, the altitude of thermal equilibrium must be well defined. Currently, the established heat equation formalism is used to

quantify the relationships between the heating and cooling processes and to predict the thermal equilibrium altitude (e.g., see Schunk and Nagy, 2009; Kelley, 2009; and Matta et al., 2014).

This paper is focused on assessing our quantitative understanding of the highest altitude below which thermal equilibrium occurs. Despite over 60 years of observations, model predictions of the altitudes where thermal equilibrium occurs have not been validated because there is not an adequate database of simultaneous electron, ion, and neutral temperatures in the collision-dominated environment of the lower ionospheres of planetary atmospheres. We have been unable to find published observations of the altitude of thermal equilibrium in the atmospheres of Earth or Mars. Simultaneous in-situ observations of the electron, ion, and neutral temperature profiles below 140 km on Earth and Mars are limited to the small number of intervals where the Atmosphere Explorer–C (AE–C; Dalgarno et al. 1973) and the Mars Atmosphere and Volatile Evolution (MAVEN; Jakosky et al. 2015) satellites were driven into unstable low orbits for intervals of a few days. Both the AE-C and MAVEN satellites used onboard propulsion to drive the perigee altitude down and back up from these unstable orbits.

A literature search has not revealed any publications presenting simultaneous altitude profiles of the electron, ion, and neutral temperatures from AE-C. However, there are archived data of AE-C that have simultaneous neutral, ion, and electron temperature profiles. Two examples are presented below. Surprisingly, there are more observations of simultaneous low-altitude ion, electron, and neutral temperature profiles at Mars from the MAVEN satellite compared with those on Earth. Analysis of the Mars temperature profiles at altitudes below 140 km have demonstrated: 1) That MAVEN data are not consistent with a plasma characterized by electrons in thermal equilibrium with the neutral population above 100 km (Peterson et al. 2020) and 2). The source of energy maintaining high ion temperatures at low altitudes on Mars has not been identified (Hanley et al. 2021). Further analysis by Ergun et al. (2021) shows that CO_2 excitation/de-excitation of its lowest-energy vibrational states dominates energy transfer to and from electrons. Additionally, Andersson et al. (2019) have detected an unexpected and unexplained electron temperature spike in the lower dynamo region of the Mars ionosphere. We are unsure if features such as those found in the lower ionosphere of Mars exist in the Earth's ionosphere since there is not an adequate database of simultaneous electron, ion, and neutral temperature profiles.

On Earth, ground-based incoherent/collective Thomson radar scattering facilities routinely obtain altitude profiles of electron and ion temperatures (e.g., Mahajan, 1967, Evans 1969). However, there are significantly fewer published altitude profiles of the neutral temperature. Most of the published neutral temperature altitude profiles are obtained from scans of far ultraviolet radiances observed on the Earth's limb (e.g., Meier et al. 2015). We could not find any publications presenting neutral temperature profiles extending below 200 km obtained over an operating incoherent scatter radar. However, Zhang et al. (2005) presented and analyzed neutral temperature profiles obtained by the TIMED/GUVI instrument (Christensen et al. 2003) above 200 km with ion and electron temperature profiles obtained above 150 km by the Millstone Hill incoherent scatter radar. Extensive archives of both TIMED/GUVI and Millstone Hill radar observations exist. We identified multiple intervals where temporally and near spatially coincident temperature profiles were available in these archives. Two examples are presented and discussed below.

There are many physics-based models of the Earth's ionosphere that can predict the altitude of thermal equilibrium under various solar and geophysical conditions. For example, the Whole Atmosphere Community Climate Model with thermosphere and ionosphere extension (WACCM-X 2.0) (Liu et al. 2018), the NCAR Thermosphere-Ionosphere-Electrodynamics General Circulation Model (TIE-GCM) (Qian et al. 2014), SAMI3 is another model of the Ionosphere (SAMI3) (Huba and Drob, 2017), the Coupled Thermosphere-Ionosphere-Plasmasphere model, CTIP (Millward et al. 1996), the whole Atmosphere Model with Ionosphere, Plasmasphere, Electrodynamics WAM-IPE, (Hysell et al. 2022), and the Field Line Interhemispheric Plasma (FLIP) model (Richards et al. 2009).

This paper analyzes sub-solar neutral, ion, and electron temperature profiles from the archives of AE-C, TIMED/GUVI, and the Millstone Hill Incoherent scatter radar. To minimize ionospheric storm effects, temperature profile data were selected equatorward of the auroral zone during geomagnetically quiet intervals and compared with model results from the TIE-GCM and FLIP models.

Data and Models

AE-C Satellite

The Atmosphere Explorer (AE) mission was designed to "make cause and effect studies and carry out the simultaneous measurements that are needed to achieve a detailed understanding of the physical processes that govern the lower thermosphere and ionosphere" (Dalgarno et al. 1973). AE-C is the only spacecraft with simultaneous observations of neutral, ion, and electron temperatures below 140 km on Earth. It was launched in December 1973 into a 150 × 4294 km, 68^{o} inclination orbit. Onboard propulsion was used in 1974 to temporarily lower perigee and sample altitudes below 150 km. Neutral temperatures were obtained from the Neutral Atmosphere Temperature Experiment (NATE) instrument (Spencer et al. 1973), ion temperatures were obtained by the Retarding Potential Analyzer (RPA) instrument (Hanson et al. 1973), and electron temperatures were obtained by the Cylindrical Electrostatic Probe (CEP) instrument (Brace et al. 1973). Total plasma densities were obtained by both the CEP and RPA instruments. Selected data from all the AE-C instruments at a 15-second cadence were collecteted into a Unified Abstract (UA) file and archived by NASA. Data from the UA file are used here.

TIMED/GUVI

The Thermosphere Ionosphere Mesosphere Energy and Dynamics (TIMED) satellite was launched in December 2001 into a 630-kilometer circular orbit inclined at 74.1º. Christensen et al. (2003) describe the Global UltraViolet Imager (GUVI) instrument and some initial results. Meier et al. (2015) describe the methods used to obtain neutral temperature altitude profiles and error estimates from the limb scan data. Limb scan and other data products are archived at the Johns Hopkins Applied Physics Laboratory. The APL archives contain data from February 23, 2002 through December 12, 2007, with data gaps associated with instrument and satellite operations. Data for orbits where the limb scan was within 7^{o} of latitude and 15^{o} of longitude of the Millstone Hill radar were used in the analysis presented here.

Millstone Hill (MH) Incoherent Scatter Radar

The Millstone Hill (MH) incoherent scatter radar is located at 42.6º North, 71.5º West and has been operated as a community ionospheric facility for more than 5 solar cycles. Ion density and electron and ion temperature profiles are obtained at varying time cadence from the power spectrum of averaged radar pulse returns as described by e.g. Evans (1969). Collective Thomson/incoherent scatter is a random process where thermal electrons, electrostatically modified by the presence of ions, provide a very weak radar backscatter target. The random nature of the scatter requires that many spectra are averaged in time to identify up and down shifted peaks associated with the ion acoustic plasma resonance frequency, which is proportional to the square root of the ratio of the ion temperature to mass. The detailed shape of the up/downshifted lines is related to the ratio of the electron and ion temperature. Ion temperature is obtained from a spectral fitting code that includes a model of ion composition as a function of altitude. Depending on the time delay (altitude) of the return, different types of radar pulses, averaging times, and altitude binning are used. Consequently, there are many data products available from the Millstone Hill (MH) radar archived data in the Madrigal distributed database operated by the facility. In this study, we use the 15-minute cadence gridded data product in Madrigal, which provides electron and ion temperature profiles consistently at a fixed temporal and spatial resolution and with data coverage encompassing the 5 years of GUVI operation.

FLIP ionospheric model

The field line interhemispheric plasma (FLIP) model is a one-dimensional model that calculates the plasma densities and temperatures along magnetic flux tubes from below 100 km in the Northern Hemisphere through the plasmasphere to below 100 km in the Southern Hemisphere (Richards 2001; Richards et al. 2010). A detailed description of the FLIP model can be found in the paper by Kotov et al. (2015). The only significant update since 2015 is the adoption of the latest Magnetic Apex coordinates instead of tilted dipole coordinates (Van Zandt et al. (1972), Richmond (1995)).

The FLIP model solves the continuity and momentum equations for O^+, H^+, He^+, and N^+ along entire field lines. Many other ion densities are calculated from local chemical equilibrium. The chemical reaction rates were validated using AE satellite data (Richards, 2011). The ion and electron temperatures are obtained by solving time-dependent energy equations that are based on the work of Schunk and Nagy (1978). For the neutral atmosphere, including the netural temperature, the FLIP model uses the NRL Mass Spectrometer, Incoherent Scatter Radar Extended model (NRLMSISE-00) (Picone et al. 2002).

The photoionization calculations in this paper use a model of solar EUV irradiances based on measurements by the Solar Extreme Ultraviolet Experiment (SEE) instrument on the TIMED satellite (Woods et al. 2008). The SEE irradiances produce very good agreement between the measured and modeled NmF2 during the 2006-2009 solar minimum period (Richards et al. 2009, 2010, 2014). The heating of thermal electrons by photoelectrons is determined by the solution of the two-stream photoelectron flux equations along entire field lines using the method of Nagy and Banks (1970).

TIE-GCM model

The Thermosphere-Ionosphere-Electrodynamics General Circulation Model (TIE-GCM) "self-consistently solves the fully coupled, nonlinear, hydrodynamic, thermodynamic, and continuity equations of the neutral gas, the ion and electron energy and momentum equations, the ion continuity equation, and neutral wind dynamo" (e.g., Qian et al. 2014). Effects of turbulent mixing caused by gravity wave breaking are implicitly included by specifying an eddy diffusivity (Roble et al. 1987). TIE-GCM uses the Apex Coordinates and take inputs of F10.7 cm solar radio flux and Kp index. TIE-GCM self-concistently calculates the neutral temperature in addition to electron and ion temperatures above the lower boundary at 97 km at which the model reads in the temperature values from the history input file. The vertical level spacing is 0.5 points each scale height (~7km). Furthermore, photoelectron flux and the corresponding photoelectron heating rate for thermal electrons is calculated self-consistently with plasma densities and temperatures in FLIP every time step whereas TIE-GCM assumes the heating rate to be proportional to the photoionization rate using the efficiency factor (Swartz and Nisbet, 1972; Smithtro & Solomon, 2008; Smithtro & Sojka, 2005). We have used the runs-on-request feature of the NASA Community Coordinated Modeling Center (CCMC) to produce the model results shown in Figure 2.

Results

Atmosphere Explorer

Figure 1 compares modeled and *in-situ* altitude profile data for plasma density and the ion, electron, and neutral temperatures from AE-C orbits 2929-downleg (top row) and 2935 (bottom row) during a geomagnetically quiet interval. The data from the upleg and downleg of orbit 2929 are not significantly different. The times, latitudes, and longitudes of perigee were 1974-08-25/20:09:00 and 1974-08-26/07:13:45, -3.4^{o} and -3^{o}, and 82^{o} W and 110.5^{o} E, respectively. The magnetic activity was low, the planetary magnetic indices (A_P) being 6 and 4, and the $F_{10.7}$ indices were 75.7 and 73 for the two passes. The perigee near the geographic equator was chosen because the temperatures are least likely to be affected by geomagnetic activity there.

Panels A, B, D, and E report observed and modeled values from 100 to 250 km. Panels A and D show the plasma density as a function of altitude from the CEP instrument as plus (+) signs, from the RPA instrument as asterisks (*), and the FLIP model as dashed lines. Panels B and E show CEP electron temperatures (Te) as black plus (+) signs, RPI ion temperatures (Ti) as red multiplication (×) signs, and NATE neutral temperatures (Tn) as blue boxes. The dashed lines are FLIP model temperatures for electrons (black), ions (red), and neutrals (blue).

Temperature differences from 100 to 150 km are shown in panels C and F. The observed Te-Tn values are shown as black plus (+) signs, and the observed Ti-Tn values are shown as red asterisks (*). The FLIP model results are shown as black dashed lines for Te-Tn, and red dashed lines for Ti-Tn (which are negligible).

Observational uncertainties are not shown because the literature has only qualitative discussions of the uncertainties in the AE-C instruments. The equatorial perigee passes sample

different latitudes and longitudes on the inbound and outbound portions of orbit 2935 (bottom row). Unlike orbit 2929, this results in significantly different temperatures and densities at nearly identical altitudes for orbit 2935. The RPA ion density measurements were systematically 40% larger than the CEP measurements at the lowest altitudes. The FLIP model densities are typically within 10% of the RPA values.

The FLIP model calculations shown in Figure 1 were performed along separate field lines corresponding to each data point along the satellite orbit. The model results are close to the observed electron, ion, and neutral temperature profiles below 250 km. Because of the strong energy coupling, the FLIP model calculated electron and ion temperatures are sensitive to the NRLMSISE-00 empirical model neutral temperatures. Observed neutral temperatures on both orbits shown in Panels B and E are slightly lower than the NRLMSISE-00 values. The difference between observed neutral and ion temperatures above 150 km is larger than that predicted by the FLIP model. The model calculations are most accurate in these low-altitude equatorial regions because vertical ion motion and vertical energy flow are restricted by the near horizontal field lines. This means that plasma and energy transport uncertainties are negligible, and the densities and temperatures should be close to their local equilibrium values. Away from the equatorial region, downward heat flow significantly contributes to model temperature uncertainty, even below 200 km.

The observed ion temperatures are lower than the neutral temperatures on orbit 2935, below about 145 km (Figure 1, Panel F). Given our current understanding of the rapid transfer of heat between ions and neutrals, we expect the ion temperature to lie between the electron and neutral temperatures and to be within a few degrees of the neutral temperature below 200 km altitude. The model results from FLIP (red dashed lines in Panels C and F) show nearly equal ion and neutral temperatures below 150 km. Instrumental uncertainty or spatial/temporal aliasing is the probable explanation that the observed ion temperature is lower than the nearly coincident observed neutral temperature. The AE-C in-situ neutral temperatures were obtained from a quadrupole mass spectrometer using both a baffle and velocity scan techniques (Spencer et al. 1973). Neutral temperatures from state-of-the-art quadrupole mass spectrometers (e.g., the MAVEN NGIMS instrument, Mahaffey et al. 2015) now provide higher temporal resolution by integrating a non-reactive gas' density profile assuming hydrostatic balance (e.g., Stone et al. 2018, Snowden et al. 2013).

The temperatures shown in Figure 1 and the temperature differences in panels C and F demonstrate that thermal equilibrium between the ions, electrons, and the neutrals occurs below 135 km, the lowest altitude sampled by the AE-C spacecraft.

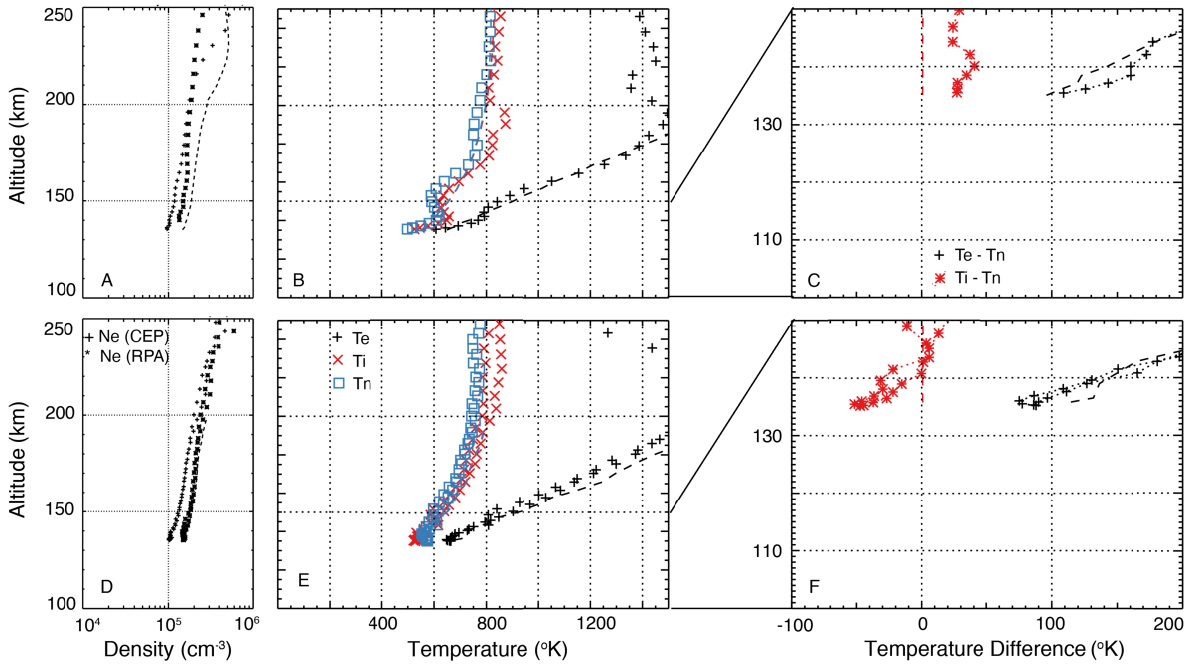

Figure 1: Modeled and Atmosphere Explorer-C satellite plasma density and ion, electron, and neutral temperature altitude profiles from orbits 2929 (upper row) and 2935 (lower row) on August 25 and 26, 1974, respectively. FLIP model calculations are denoted by dashed lines, and observations are denoted by symbols. Panels A and D show plasma densities; Panels B and E show electron, ion, and neutral temperatures; Panels C and F report ion-neutral and electron-neutral temperature differences below 150 km. See text for more details.

Millstone Hill Ionospheric Radar

Figure 2 presents observed and modeled temperature and density profiles on March 8, 2006, over the Millstone Hill (MH) incoherent scatter radar (ISR) at 43°N, 288°E, along with TIMED/GUVI limb scans from orbits 23006 (top row) and 23007 (bottom row). Geomagnetic conditions were quiet for both intervals. The planetary magnetic (A_P) index was 4, and the solar $F_{10.7}$ index was 71.5 for both intervals.

The observed and modeled values shown in Figure 2 are not exactly spatially and temporally coincident. Gridded Te, Ti, and density data from the MH radar archives for the interval 18:45 to 19:00 UT are shown in the top row and from 20:30 to 20:45 UT in the bottom row. The neutral temperature profiles are from GUVI limb scans. The tangent longitudes at the lowest altitude of the GUVI scan were 11.0° east of MH on orbit 23006 at 18:53:38 UT and 13.5° west of MH on orbit 23007 at 20:30:30 UT. The tangent latitudes were equal to those of MH. The FLIP model calculations were carried out for 19:00 (top row) and 20:30 UT (bottom row) along magnetic field lines that go through a point 250 km altitude directly above Millstone Hill.

Panels A, B, D, and E report observed and modeled density and temperature values from 100 to 250 km. Panels A and D report plasma density as a function of altitude. MH data are shown as plus (+) signs; the FLIP model results as dashed lines; and the TIE-GCM model results

as solid lines. Panels B and E show temperature profiles of Te (black), Ti (red), and Tn (blue). Observations of Te are shown as black plus (+) signs, Ti as red multiplication (×) signs, and Tn as blue boxes. One-sigma error ranges are shown as horizontal lines for neutral (blue) and ion (red) temperatures. Error ranges for electron temperature are available but not shown. As explained by Evans (1969), uncertainties in the electron temperature are larger than the uncertainties in the ion temperature. Note that the FLIP model calculation indicates that the atomic to molecular ion density ratio is too small to affect the accuracy of the ISR Te analysis below ~170 km altitude.

Panels A and D show that the TIE-GCM model slightly underestimates the ISR density above 200 km, whereas the FLIP model matches the ISR density well. Both models progressively underestimate the density below 150 km. This underestimation of the E-region density is a well-known problem with models. Panels B and E show that both models agree well with the measured ion temperature, and they give electron temperatures that are higher by ~130^{o}K (11%) on average above 150 km altitude.

Panels C and F report the observed and modeled temperature differences from 100 to 150 km. Te-Tn values are color-coded black; Ti-Tn values are color-coded red. Observed Te-Tn values are shown as plus (+) signs; Ti-Tn are shown as asterisks (*). The horizontal red lines show the 1 sigma uncertainty of the difference between the ion and neutral temperatures. FLIP model results are dashed lines, and TIE-GCM model results are solid lines. Observationally there are extended altitude ranges for both intervals where the measured ion and electron temperatures are lower than the neutral temperatures. The most probable explanation for ion temperatures being lower than the nearly coincident neutral temperatures is that these temperatures varied on temporal and spatial scales shorter than those sampled by the MH radar and by GUVI limb scans.

Ultimately, the error bars on the temperature observations presented in Figure 2 do not allow a strong conclusion about the altitude of thermal equilibrium other than it is below ~140 km. The TIE-GCM (solid lines) and FLIP (dashed lines) model runs predict the highest altitude of thermal equilibrium in these events is at ~115 km. The observations shown cannot confirm or refute the model results.

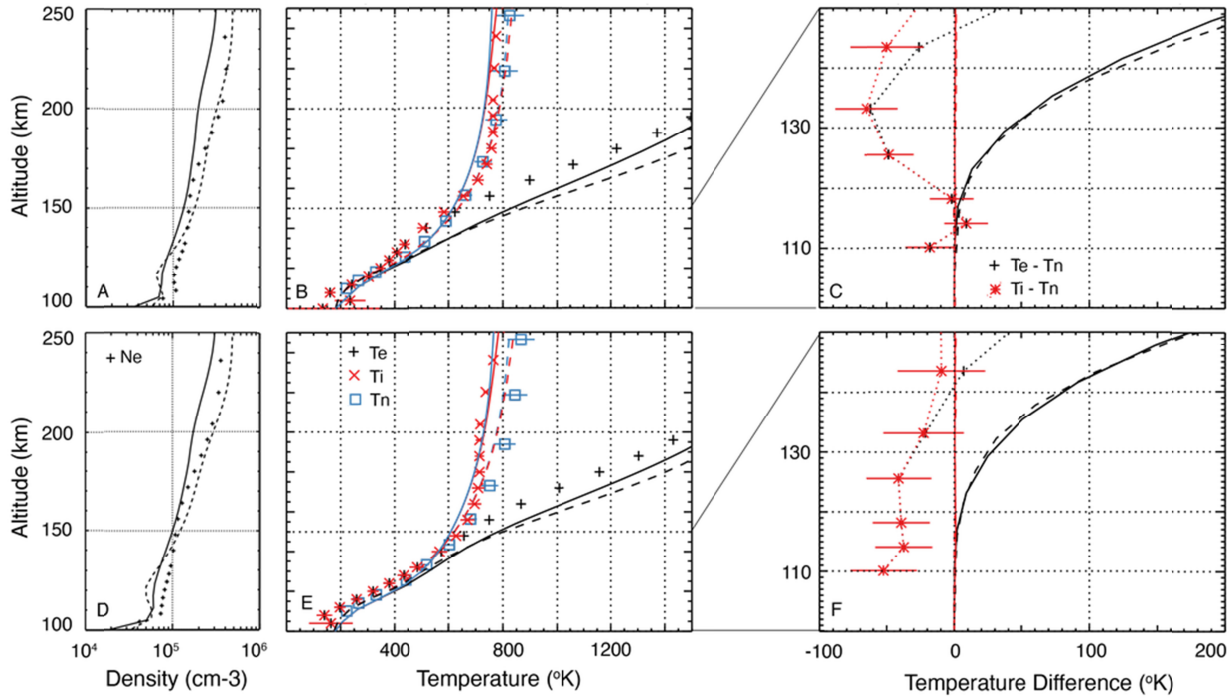

Figure 2. Nearly coincident modeled and observed temperature and density profiles on March 8, 2006, from the Millstone Hill incoherent scatter radar and TIMED/GUVI limb scans from orbits 23006 (top row) and 23007 (bottom row). The model results are along field lines at MH for 19:00 (top row) and 20:30 (bottom row). Observations are denoted as symbols and TIE-GCM and FLIP model results as solid and dashed lines, respectively. Panels A and D show plasma densities; Panels B and E show electron, ion, and neutral temperatures; Panels C and F report ion-neutral and electron-neutral temperature differences. See text for remaining details.

Discussion

Observing and predicting the altitude of thermal equilibrium in the daytime ionosphere is a basic test of our understanding of energy transfer from solar EUV radiation to the neutral atmosphere. Some of the earliest observations of the space age unexpectedly showed that the electron temperature was higher than the ion and neutral temperature in the daytime ionosphere and thus demonstrated that photoelectrons were heating the thermal electrons (e.g., Lejeune and Petit, 1969) faster than they could cool. Observing and quantitatively understanding the transfer of energy from the solar EUV-generated photoelectrons to the ions and neutrals was a goal of the AE project in the 1970's. This goal has only been partially attained.

At high latitudes, in the auroral zone, polar cap, and magnetospheric cusp regions, energy input from solar EUV radiation is often not the most significant energy source. That is why we focus on sub-auroral latitudes during geomagnetically quiet intervals where high latitude processes such as Joule heating do not contribute to neutral and ion heating.

Figures 1 and 2 show examples of ion, electron, and neutral temperature profiles obtained at sub-auroral latitudes during geomagnetically quiet intervals from public data archives. These

profiles demonstrate that there is not yet a quantitative understanding of the altitude where thermal equilibrium occurs. Current ionosphere/thermosphere models generally agree with the electron, ion, and neutral temperature profiles, as shown in Figures 1 and 2. These models predict altitudes for thermal equilibrium, but these predictions have yet to be validated with an adequate observational database of simultaneous ion, electron, and neutral temperatures in the altitude range below ~135 km where thermal equilibrium occurs.

There are no simultaneous *in-situ* neutral, ion, and electron temperature measurements near the expected altitude of thermal equilibrium. The observations from the AE-C mission in Figure 1 and those from the Mars MAVEN mission (Hanley et al. 2021) illustrate that current missions cannot get to the altitude of thermal equilibrium. Sarris et al. (2020) address the many technical and programmatic issues that need to be resolved to produce a mission that can obtain *in-situ* neutral, ion, and electron temperature profiles closer to the altitude of thermal equilibrium.

There are numerous simultaneous electron and ion temperature profiles in the 100 to 200 km range from radar observations discussed by Evans (1969) and many others. In this study, we have identified several near simultaneous neutral temperature profiles from EUV limb scans from TIMED/GUVI over the MH radar site when archived data exist. Two examples are presented in Figure 2. The different spatial and temporal scales of neutral temperature profiles from limb observations and the ion and electron temperature profiles from the MH radar introduce uncertainties in determining the altitude of thermal equilibrium. Additionally, the radar modes and codes used to obtain survey ion and electron temperature profiles shown in Figure 2 are not specifically optimized for altitudes below about 200 km. Furthermore, measurement uncertainties are limited by the radar's design specifications (e.g. power-aperture product) as well as the timescale of inherent ionospheric variability, as this limits the maximum averaging time that can be used to maintain statistical, stationary conditions and hence sets a floor on temperature uncertainties.

The FLIP and TIE-GCM model temperature profiles agree well with the available observations, but the uncertainties and poor spatial/temporal overlap of existing remote sensing observations, such as those presented in Figure 2, are not adequate to place strong constraints on the models. Radar observations can be optimized to be more precise below 140 km within design limitations. Neutral temperatures from UV limb scan technology from future satellites can be better coordinated with ground radar sites and their operational modes.

Temperature profiles in Figures 1 and 2 show altitude ranges where the observed ion temperatures are significantly lower than the observed neutral temperatures. We note that neither our current physical understanding nor either model predicts any instances where $T_i < T_n$. As stated above, the probable reason for these unexpected cool ion temperatures (or unexpected warm neutral temperatures) comes from the limitations of the observational techniques. A closely related explanation could be that either the ion or neutral temperatures vary significantly on temporal and/or spatial scales smaller than those of the observations. The intervals selected for analysis, however, were chosen to be from geomagnetically quiet intervals equatorward of the auroral oval where significant spatial and temporal variations in the neutral atmosphere and ionosphere that could produce the results shown in Figures 1 and 2 are not expected.

The data and analysis presented here cannot determine if the examples of Ti < Tn in three of the four temperature profiles presented in Figures 1 and 2 are real. As suggested in the previous paragraph they most probably are the result of instrumental and observational limitations. However, if the observations of Ti < Tn in the 100-130 km range are real and commonly occur, they would result from unexpected and unexplored physical processes. A candidate process might include large amplitude, high altitude gravity waves (e.g., England et al. 2020). A quantitative understanding of sub-solar temperature profiles in the 100-130 km range based on validated models and observations does not exist, so we are left with the possibility that regions where Ti < Tn can occur in the 100-130 km range.

Conclusions

Systematically investigating and modeling the processes that heat neutrals above the mesopause and below the altitude of thermal equilibrium requires a robust understanding of the upper boundary conditions on those processes, such as ion, electron, and neutral temperature profiles in the 100-130 km range.

The data and analysis presented here show that the altitude of thermal equilibrium, where the electron, ion, and neutral temperatures are equal, as well as its variability under various geophysical conditions, has not yet been observationally established. It follows that models predicting this altitude at sub-auroral latitudes during geomagnetically quiet intervals have not been validated. This is because *in-situ* and remote sensing of simultaneous ion, electron, and neutral temperature profiles in the 110 to 140 km range with sufficient resolution to identify the altitude at thermal equilibrium is challenging.

Progress in quantitatively understanding neutral heating and the altitude of thermal equilibrium at sub-auroral latitudes during geomagnetically quiet intervals in the 80 to 140 km region requires new robust measurements of neutral, ion, and electron temperature profiles with subsequent model validation.

Acknowledgements

WKP acknowledges helpful discussions with Panos Pirnaris, Theodore Saris, Gwen Hanley, Richard Eastes, Bill McClintock, Phil Chamberlin, Tom Woods, Skylar Shaver, Marcin Pilinski, Katelynn Greer, and Laila Andersson. We thank NASA's Community Coordinated Modeling Center (CCMC) for providing access to the TIE-GCM model via its runs on request service. WKP was supported by NASA Grant 80NSSC20K0594. AWY was supported by Canadian Space Agency Grant 16SUSTSSPI. PGR is comfortably retired. PJE support for radar operations and analysis at the Millstone Hill Geospace Facility, and the Madrigal distributed database system archiving these observations, are provided to the community by the Massachusetts Institute of Technology under a series of National Science Foundation grants including AGS-1952737.

Open Research:

Data presented here are from public data archives. Atmosphere Explorer–C data are available at https://omniweb.gsfc.nasa.gov/ftpbrowser/ae_c.html. Millstone Hill radar data are archived on the Madrigal system and can be found at: http://millstonehill.haystack.mit.edu/. The GUVI Level 2B neutral density profile IDL save sets used here are documented in the file: http://guvitimed.jhuapl.edu/sites/default/files/data/documents/readme_GUVI_Version_13_Limb_Retrievals.pdf. They are available at: http://guvitimed.jhuapl.edu/data_fetch_l2b_ndp_idlsave. The FORTRAN source code for the FLIP software used in this research is available from PGR upon request.

References:

Andersson, L, Christopher Fowler, Bob Ergun, Roger Yelle, Thomas Edwards Cravens, Ed Thiemann, et al. (2019), Hot electron temperature layer in the Martian atmosphere, ESSOAR, https://doi.org/10.1002/essoar.10501096.1

Brace, L.H., R.G. Theis, and A. Dalgarno (1973), The cylindrical electrostatic probes for Atmosphere Explorer –C, -D, and –E, Radio Science, 8,341-348, https://doi.org/10.1029/RS008i004p00341

Christensen, A. B., et al. (2003), Initial observations with the Global Ultraviolet Imager (GUVI) in the NASA TIMED satellite mission, J. Geophys. Res., 108(A12), 1451, doi:10.1029/2003JA009918.

Dalgarno, A, W.B. Hanson, N.W. Spencer, and E.R. Schmerling (1973), The Atmosphere Explorer mission, Radio Science, 8, 263-266, https://doi.org/10.1029/RS008i004p00263

England, S. L., Greer, K. R., Solomon, S. C., Eastes, R. W., McClintock, W. E., & Burns, A. G. (2020). Observation of thermospheric gravity waves in the Southern Hemisphere with GOLD. Journal of Geophysical Research: Space Physics, 125, e2019JA027405. https://doi.org/10.1029/2019JA027405

Ergun, R. E., Andersson, L. A., Fowler, C. M., Thaller, S. A., & Yelle, R. V. (2021). In-situ measurements of electron temperature and density in Mars' dayside ionosphere. *Geophysical Research Letters*, 48, e2021GL093623. https://doi.org/10.1029/2021GL093623

Evans, J.V. (1969), Theory and Practice of Ionosphere Study by Thomson Scatter Radar, Proceedings of the IEEE, 57, 496

Hanley, K. G., McFadden, J. P., Mitchell, D. L., Fowler, C. M., Stone, S. W., Yelle, R. V., et al. (2021). In situ measurements of thermal ion temperature in the Martian ionosphere. Journal of Geophysical Research: Space Physics, 126, e2021JA029531. https://doi.org/10.1029/2021JA029531

Hanson, W.B., D.R. Zuccaro, C.R. Lippincott, and S. Sanatani (1973), The retarding-potential analyzer on Atmosphere Explorer, Radio Science, 8, 333-340, https://doi.org/10.1029/RS008i004p00333

Heelis, R. A., & Maute, A. (2020). Challenges to understanding the Earth's ionosphere and thermosphere. Journal of Geophysical Research: Space Physics, 125, e2019JA027497. https:// doi.org/10.1029/2019JA027497 doi.org/10.1029/2019JA027497

Huba, J. D., and Drob, D. (2017), SAMI3 prediction of the impact of the 21 August 2017 total solar eclipse on the ionosphere/plasmasphere system, *Geophys. Res. Lett.*, 44, 5928–5935, doi:10.1002/2017GL073549.

Hysell, D. L., Fang, T. W., & Fuller-Rowell, T. J. (2022). Modeling equatorial *F*-region ionospheric instability using a regional ionospheric irregularity model and WAM-IPE. *Journal of Geophysical Research: Space Physics*, 127, e2022JA030513. https://doi.org/10.1029/2022JA030513

Jakosky, B.M., R.P. Lin, J.M. Grebowsky, J.G. Luhmann, D.F. Mitchel et al. (2015), The Mars Atmosphere and Volatile Evolution (MAVEN) Mission, Space Sci. Rev., 195:3-48.

Jones Jr., McArthur, J.T. Emmert, Quan Gan, and Jia Yue, (2022), On the importance of neutral composition and temperature measurements in the 100–200 km altitude region, Front. Astron. Space Sci., 29 November 2022, https://doi.org/10.3389/fspas.2022.1062967.

Kelley, Michael C. (2009), The Earth's Ionosphere: Plasma Physics and Electrodynamics, Second Edition, Elsevier, ISBN 13: 978-0-12-088425-4

Kotov, D., V. Truhlík, P. G. Richards, S. Stankov, O. V. Bogomaz, L. F. Chernogor, I. F. Domnin, Night-time light ion transition height behaviour over the Kharkiv (50°N, 36°E) IS radar during the equinoxes of 2006–2010, J. Atmos. Solar-Terr. Phys, http://dx.doi.org/10.1016/j.jastp.2015.06.004, 1364-6826, 2015.

Lejeune, G. and M. Petit (1969), A study of the daytime electron temperature, Planet. Space Sci., 17,1763-1780, https://doi.org/10.1016/0032-0633(69)90053-1

Liu, H.-L., Bardeen, C. G., Foster, B. T., Lauritzen, P., Liu, J., Lu, G., . . . Wang, W. (2018). Development and validation of the Whole Atmosphere Community Climate Model with thermosphere and ionosphere extension (WACCM-X 2.0). Journal of Advances in Modeling Earth Systems, 10, 381–402. https://doi.org/10.1002/2017MS001232

Matta, M., M. Galand, L. Moore, M. Mendillo, and P. Withers (2014), Numerical simulations of ion and electron temperatures in the ionosphere of Mars: Multiple ions and diurnal variations, Icarus, 277, 78-88, https://doi.org/10.1016/j.icarus.2013.09.006.

Mahaffy, P. R., Benna, M., King, T., Harpold, D. N., Arvey, R., Barciniak, M., et al. (2015). The neutral gas and ion mass spectrometer on the Mars atmosphere and volatile evolution mission. Space Science Reviews, 195(1-4), 49–73. https://doi.org/10.1007/s11214-014-0091-1

Mahajan, K.K., (1967), Extent of non-equilibrium in the ionosphere, J. Atmos. And Terrestrial Phys, 29, 1137-1151.

Meier R. R., et al. (2015) Remote Sensing of Earth's Limb by TIMED/GUVI: Retrieval of thermospheric composition and temperature, Earth and Space Science, 2, 1–37, doi: 10.1002/2014EA000035.

Millward, G. H., R. J. Moffett, S. Quegan, and T. J. Fuller-Rowell, A coupled thermosphere-ionosphere-plasmasphere model (CTIP), in STEP Handbook on Ionospheric Models, Ed. R. W. Schunk, Utah State University, 239, 1996.

Nagy, A. F., and P. M. Banks (1970), Photoelectron fluxes in the ionosphere, J. Geophys. Res., 75(31), 6260–6270.

Palmroth, M. et al. (2020), Lower-thermosphere–ionosphere (LTI) quantities: current status of measuring techniques and models, Ann. Geophys., 39, 189-237, https://doi.org/10.5194/angeo-39-189-2021

570 Peterson, W. K., Andersson, L., Ergun, R., Thiemann, E., Pilinski, M., Thaller, S., et al (2020).
571 Subsolar electron temperatures in the lower Martian ionosphere. *Journal of Geophysical*
572 *Research: Space Physics*, 125, e2019JA027597. https://doi.org/10.1029/2019JA027597
573 Peterson WK (2021) Perspective on Energetic and Thermal Atmospheric Photoelectrons. Front.
574 Astron. Space Sci. 8:655309. doi: 10.3389/fspas.2021.655309
575 Picone, J. M., A. E. Hedin, D. P. Drob, and A. C. Aikin (2002), NRLMSISE-00 empirical model
576 of the atmosphere: Statistical comparisons and scientific issues, J. Geophys. Res.,
577 107(A12), 1468.
578 Qian, L., Burns, A.G., Emery, B.A., Foster, B., Lu, G., Maute, A., Richmond, A.D., Roble, R.G.,
579 Solomon, S.C. and Wang, W. (2014). The NCAR TIE-GCM. In Modeling the
580 Ionosphere–Thermosphere System (eds J. Huba, R. Schunk and G. Khazanov).
581 https://doi.org/10.1002/9781118704417.ch7
582 Richards, P. G. (2001), Seasonal and solar cycle variations of the ionospheric peak electron
583 density: Comparison of measurement and models, J. Geophys. Res., 106(A7), 12803–
584 12819.
585 Richards, P. G., et al. (2009), Measured and Modeled Ionospheric densities, temperatures, and
586 winds during the IPY, J. Geophys. Res., 114, A12317, doi:10.1029/2009JA014625.
587 Richards, P. G., R. R. Meier, and P. J. Wilkinson (2010), On the compatibility of satellite
588 measurements of thermospheric composition and solar EUV irradiance with ground-
589 based ionospheric electron density data, J. Geophys. Res., 115, A10309,
590 doi:10.1029/2010JA015368.
591 Richards, P. G. (2011), Reexamination of ionospheric photochemistry, J. Geophys. Res., 116,
592 A08307, doi:10.1029/2011JA016613.
593 Richards, P. G. (2012), Reevaluation of thermosphere heating by solar EUV and UV radiation,
594 Can. J. Phys., 90(8): 759-767, 10.1139/p11-109, 2012
595 Richards, P.G. (2022), Ionospheric photoelectrons: A lateral thinking approach, Front. Astron.
596 Space Sci., 22 July 2022 Sec. Space Physics, https://doi.org/10.3389/fspas.2022.952226
597 Richmond, A.D. (1995), Ionospheric electrodynamics using magnetic apex coordinages, J.
598 Geomag. Geoelectr., 47, 192-212, https://doi.org/10.5636/jgg.47.191
599 Roble, R. G., Ridley, E. C., and Dickinson, R. E. (1987), On the global mean structure of the
600 thermosphere, *J. Geophys. Res.*, 92(A8), 8745– 8758, doi:10.1029/JA092iA08p08745.
601 Sarris, T.E. et al, (2020), Daedalus: a low-flying spacecraft for in situ exploration of the lower
602 thermosphere–ionosphere, Geosci. Instrum. Method. Data Syst., 9, 153-191,
603 https://doi.org/10.5194/gi-9-153-2020
604 Schunk, R. W., and A. F. Nagy (1978), Electron Temperatures in F-Region of Ionosphere –
605 Theory and Observations, Reviews of Geophysics, 16(3), 355–399.
606 Schunk, Robert and Andrew Nagy (2009), Ionospheres: Physics, Plasma Physics, and Chemistry,
607 Second Edition, Cambridge University Press, ISBN: 978-0-521-87706-0
608 Spencer, N.W., H.B. Niemann and G.R. Carignan (1973), The neutral-atmosphere temperature
609 instrument, Radio Science, 8, 284-296, https://doi.org/10.1029/RS008i004p00287
610 Smithtro, C. G., and S. C. Solomon (2008), An improved parameterization of thermal electron
611 heating by photoelectrons, with application to an X17 flare, J. Geophys. Res., 113,
612 A08307, doi:10.1029/2008JA013077.
613 Snowden, D., Yelle, R. V., Cui, J., Wahlund, J.-E., Edberg, N. J. T., and Ågren, K. (2013). The
614 thermal structure of Titan's upper atmosphere, I: Temperature profiles from Cassini
615 INMS observations. Icarus, 226(1), 552–582 https://doi.org/10.1016/j.icarus.2013.06.006

Stone, S. W., Yelle, R. V., Benna, M., Elrod, M. K., & Mahaffy, P. R. (2018). Thermal structure of the Martian upper atmosphere from MAVEN NGIMS. Journal of Geophysical Research: Planets, 123, 2842–2867. https://doi.org/10.1029/2018JE005559

Smithtro, C. G., and J. J. Sojka (2005), A new global average model of the coupled thermosphere and ionosphere, J. Geophys. Res., 110, A08305, doi:10.1029/2004JA010781.

Swartz, W. E., and J. S. Nisbet (1972), Revised calculations of F region ambient electron heating by photoelectrons, J. Geophys. Res., 77, 6259.

VanZandt, T.E., Clark, W.L., and Warnock, J.M. (1972). Magnetic Apex Coordinates: A magnetic coordinate system for the ionospheric F2 layer, Journal of Geophysical Research, 77, 2406-2411.

Woods, T. N., et al. (2008), XUV photometer system (XPS): improved solar irradiance algorithm using Chianti spectral models, Solar Phys, 250, 235–267, doi:10.1007/s11207-008-9196-6.

Zhang, S.-R., et al (2005), October 2002 30-day incoherent scatter radar experiments at Millstone Hill and Svalbard and simultaneous GUVI/TIMED observations, *Geophys. Res. Lett.*, 32, L01108, doi:10.1029/2004GL020732.

Figure 1.

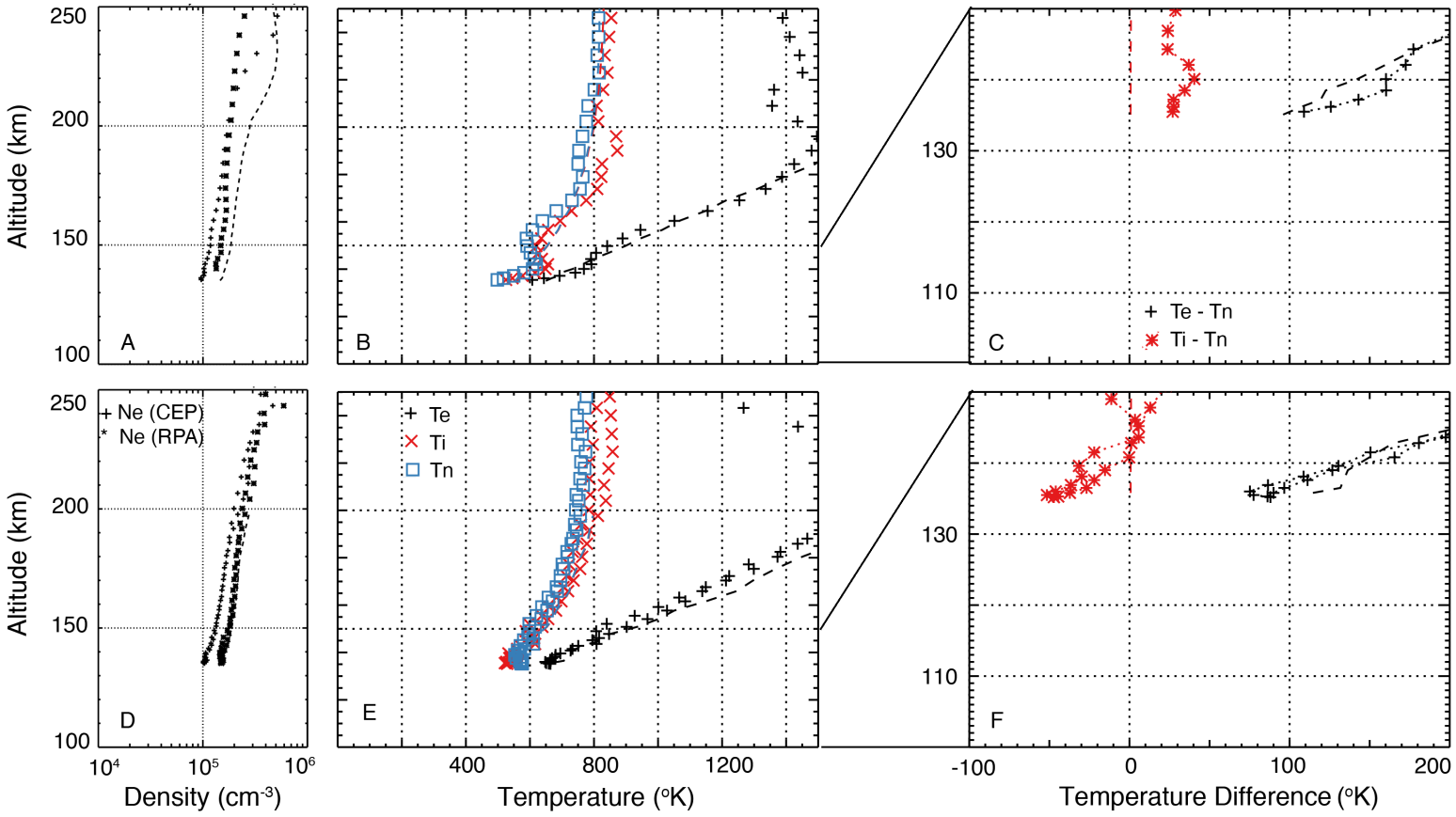
Altitude (km)
250
200
150
100
A
B
C
130
110
Te - Tn
Ti - Tn
+ Ne (CEP)
* Ne (RPA)
D
Te
Ti
Tn
E
F
10^4
10^5
10^6
Density (cm^{-3})
400
800
1200
Temperature (°K)
-100
0
100
200
Temperature Difference (°K)

Figure 2.

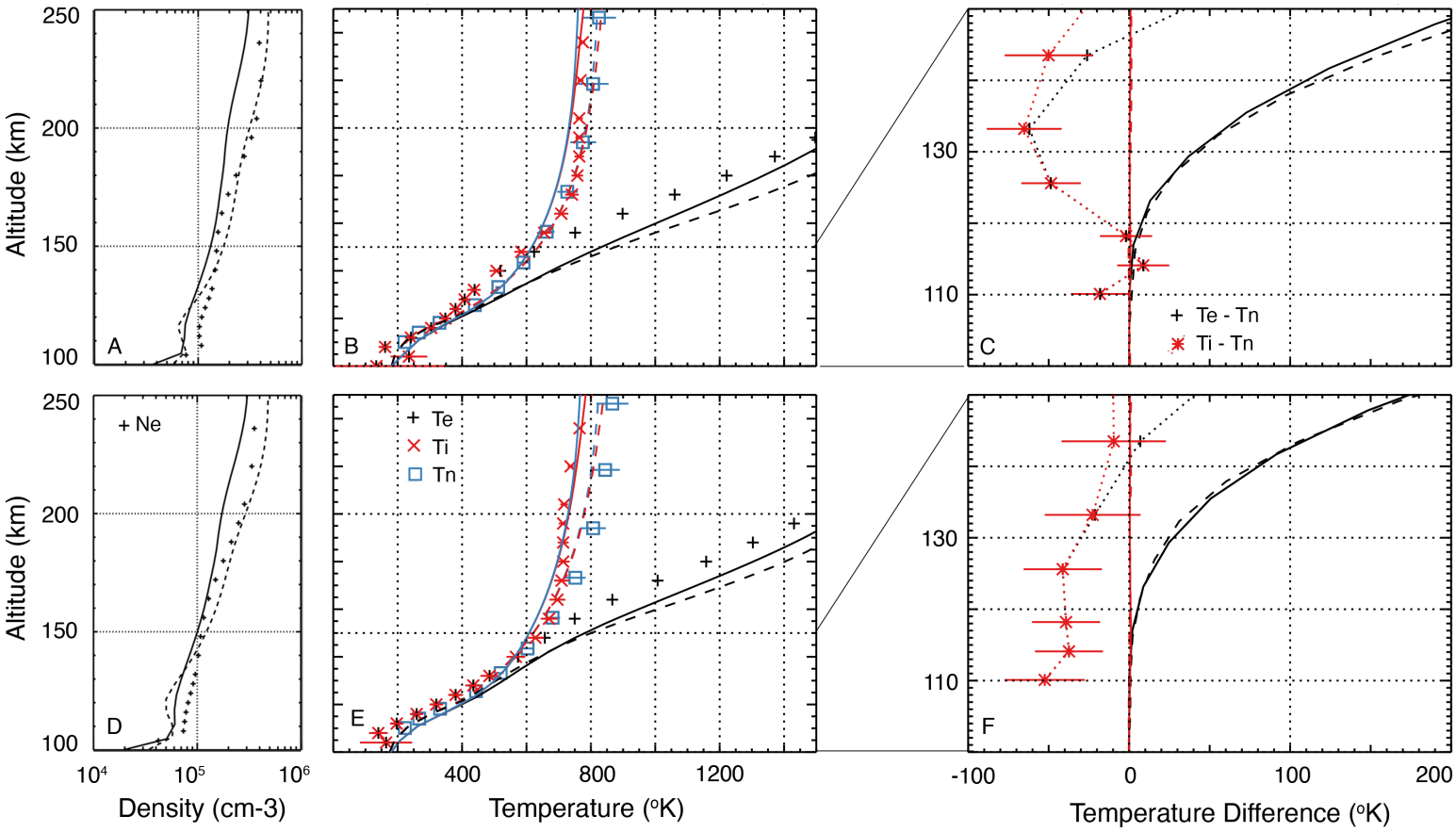
Altitude (km)
250
200
150
100
A
B
C
130
110
Te - Tn
Ti - Tn
+ Ne
D
Te
Ti
Tn
E
F
10^4
10^5
10^6
Density (cm-3)
400
800
1200
Temperature (°K)
-100
0
100
200
Temperature Difference (°K)